Droplet impingement dynamics: effect of surface temperature during boiling and non-boiling conditions

Droplet impingement dynamics: effect of surface temperature during boiling and non-boiling conditions

Jian Shen, James A Liburdy, Deborah V Pence and Vinod Narayanan

Mechanical Engineering, Oregon State University, Corvallis, OR 97331-6001, USA

Abstract

This study investigates the hydrodynamic characteristics of droplet impingement on heated surfaces and compares the effect of surface temperature when using water and a nanofluid on a polished and nanostructured surface. Results are obtained for an impact Reynolds number and Weber number of approximately 1700 and 25, respectively. Three discs are used: polished silicon, nanostructured porous silicon and gold-coated polished silicon. Seven surface temperatures, including single-phase (non-boiling) and two-phase (boiling) conditions, are included. Droplet impact velocity, transient spreading diameter and dynamic contact angle are measured. Results of water and a water-based single-wall carbon-nanotube nanofluid impinging on a polished silicon surface are compared to determine the effects of nanoparticles on impinging dynamics. The nanofluid results in larger spreading velocities, larger spreading diameters and an increase in early-stage dynamic contact angle. Results of water impinging on both polished silicon and nanostructured silicon show that the nanostructured surface enhances the heat transfer for evaporative cooling at lower surface temperatures, which is indicated by a shorter evaporation time. Using a nanofluid or a nanostructured surface can reduce the total evaporation time up to 20% and 37%, respectively. Experimental data are compared with models that predict dynamic contact angle and non-dimensional maximum spreading diameter. Results show that the molecular-kinetic theory's dynamic contact angle model agrees well with current experimental data for later times, but over-predicts at early times. Predictions of maximum spreading diameter based on surface energy analyses indicate that these models over-predict unless empirical coefficients are adjusted to fit the test conditions. This is a consequence of underestimates of the dissipative energy for the conditions studied.

(Some figures in this article are in colour only in the electronic version)

Nomenclature

Symbol

d	droplet diameter (mm)
d_o	droplet diameter prior to impact (mm)
d_{max}	maximum spreading diameter (mm)
d^*	non-dimensional droplet diameter, d/d_o
d_{max}^*	non-dimensional maximum spreading diameter, d_{max}/d_o
W_{diss}	dissipation energy (J)
E_s	surface energy (J)
E_k	kinetic energy (J)
H	droplet height (mm)
H^*	non-dimensional droplet height, H/d_o

t	time (s)
t^*	non-dimensional time, $t/(d_o/v_o)$
t_{ev}	droplet evaporation time (s)
t_{ev}^*	non-dimensional evaporation time, $t_{ev}/(d_o/v_o)$
T	temperature (°C)
$T_{s,o}$	pre-impact surface temperature (°C)
v_o	droplet impact velocity (m s^{-1})

Subscript

w	water
nf	nanofluid
p	polished surface
ns	nanostructured surface

Greek

μ	fluid viscosity (cp)

1

ρ	fluid density (kg m^{-3})
γ	surface tension (N m^{-1})
θ	contact angle (deg)
$\theta_{\text{eq-NH}}$	equilibrium contact angle, non-heated (deg)
θ^*	non-dimensional contact angle, $\theta/\theta_{\text{eq,NH}}$

1. Introduction and background

Droplet–surface impingement has been studied for well over a hundred years and there is a rich literature available on the topic. Most of the work has focused on single-droplet–surface impingement, both experimentally, numerically and theoretically. Spreading characteristics are of great importance [1–4], such as spreading diameter, crown evolution and dynamic contact angle. Important parameters include the effect of surface conditions [5, 6], such as surface roughness and surface temperatures. Droplet impinging on a heated surface is of fundamental concern for spray cooling and coating applications. Distinct stages during the evaporation process for a single impinging drop have been identified, with typically three stages being defined [7, 8]. These include stage 1: initial impact, from drop impact on the surface until flow oscillations subside; stage 2: constant contact area, during which the droplet evaporates with a pinned contact line while the contact angle decreases, during this stage most of the evaporation occurs; stage 3: constant contact angle when the contact angle reaches a critical value and the droplet continues receding with a constant contact angle. The latter two stages are also reported experimentally in [9] along with a mathematical model to determine flow and thermal fields for a evaporating sessile micro-drop on a flat heated substrate. A two-stage evaporation process is simulated in this model: constant wetting area and constant contact angle.

The hydrodynamics of droplet–surface interactions during impact and during the boiling/evaporation process are complex and very important in understanding the heat transfer process. The study by Rioboo *et al* [10] provides a detailed description of drop impact while examining a range of parameters including Reynolds number, Weber number, wettability and surface roughness. They show an initial kinematic stage that scales very well over all conditions studied which occurs when most of the drop momentum is vertical, rather than horizontal in the later stages. This initial stage occurs within less than the characteristic time defined as tV_o/d_o, where t is time, V_o the impact velocity and d_o the pre-impact diameter.

Sikalo and Ganic [11] provide a discussion of the impingement process using a scaling similar to that used in [10] and show a typical time to reach maximum spreading of the order of 1–10 times the timescale, with larger Weber numbers resulting in faster times to reach maximum spread, for fluid properties near that of water. Rioboo *et al* [10] show larger spreading diameters while keeping the Weber number constant and increasing the Reynolds number.

The splash limit is typically determined by Weber number, with Sikalo and Ganic [11] identifying an effect of surface roughness which lowers the Weber number splash limit. Droplet rebound occurs after initial spreading, eventually reaching an equilibrium diameter while oscillating with a

transient contact angle, as shown by Shen *et al* [12] and others. This complex process results in a transient film thickness near the contact line that is expected to alter the local, transient heat transfer rate.

Droplet dynamics in spray cooling has been reported by Jia and Qiu [13]. They studied the addition of surfactants to lower the droplet diameter prior to impingement. When compared with pure water, the addition of surfactants results in a lower superheat temperature for critical heat flux and a very rapid rise of heat flux with increasing surface temperature and a consequential constant heat flux beyond the critical heat flux limit. Chandra *et al* [14] looked at variations of contact angle on evaporation and measured evaporation times versus initial surface temperature. They documented the increase of heat transfer with increased wetting of the surface. Bernardin *et al* [6] identified the temperature effects on water droplet evaporation on aluminum and modeled evaporation times based on a temperature-dependent surface tension. The effect of a high resistance impact surface is shown to limit evaporation times [15].

Dynamic contact angle is one of the important parameters needed to characterize the impinging process. There are several models used to predict dynamic contact angle as a function of contact line velocity, such as the Hoffman model [16], the hydrodynamic wetting theory model [17] and the molecular-kinetic theory of wetting model [18]. Bayer and Megaridis [19] experimentally studied contact angle dynamics of water droplets impacting on smooth surfaces with widely disparate wetting characteristics, and presented the relations of dynamic contact angle and contact line velocity.

Maximum spreading diameter is also an important parameter that is predicted by several models [5, 20–22]. These models are based on surface energy analysis of the droplet before impact and at maximum spreading. The difference among these models is the estimation of dissipation energy. Chandra and Avedisian [20] developed a model to predict droplet spreading for heated droplets and simplified the dissipation energy estimation using impact velocity and the height when the drop reaches maximum diameter. Pasandideh Fard *et al* [21] estimated the dissipation energy within the boundary layer instead of using the entire height of the drop lamella. Mao and Kuhn [22] improved the P–F model by introducing empirical coefficients. These three models generally under-estimated the dissipation energy, and thereby over-predict the maximum spreading diameter. Liu *et al* [5] treated the droplet spreading as a stagnation point flow and expressed dissipation energy due to friction. They also considered the influence of surface roughness, adding a surface roughness term in the energy balance. With the empirical coefficient correlated with their experimental data, the prediction of maximum diameter agreed well.

A detailed review of models associated with drop impact is given by Yarin [23]. The ability of an energy-based model to properly predict spreading has been questioned [24]. The ability to predict the complex flow associated with the rim is generally neglected in the energy-based models, whereas a self-similar velocity distribution in the lamella has been identified based on numerical simulations. This is then used

to determine a better prediction for high Reynolds and Weber numbers.

Micro-structured surfaces, such as straight, cubic and pyramid fins, have been shown to enhance heat transfer during spray cooling compared with smooth surfaces [25–28]. Four regimes have been identified: flooded, thin film, partial dry-out and dry-out. The micro-structures are most suited in the thin film and partial dry-out regimes because of the wetting enhancement. Sodtke and Stephan [28] demonstrated that micro-structured surfaces lead to increased contact line length and thereby increases the overall heat flux. Li and Peterson [29] studied the influence of a micro-porous coated surface in pool boiling, concluding that improved wetting area in the micro-porous coating enhances overall heat transfer and that the wall superheat also occurs over a narrower range during boiling than for a smooth surface. Sriraman and Banerjee [30] extended pool boiling studies to nanostructured silicon surfaces. A significant enhancement, of the order of 40% for a given wall superheating, was observed.

Some recent studies show that the use of nanofluids is a promising option for heat transfer enhancement. However, this is not conclusive and the mechanisms for enhancement are still not fully understood. Das and Kumar [31] give a general review of the cooling potential of nanofluids and suggested that these fluids may have a significant impact on cooling. Other studies have been designed to improve the understanding, and to quantify, how thermal properties may be affected by the presence of nanoparticles in liquids [32–34]. To the authors' knowledge there are no studies in the literature concerning droplet impingement dynamics of nanofluids.

The objectives of the current study are to experimentally explore the hydrodynamic characteristics of an individual droplet impinging on a heated surface at various surface temperatures using high speed imaging. The study also investigates the effect of nanofluids and nanostructured surfaces using a single-wall carbon-nanotube (SWCNT) nanofluid and a nanoporous structured surface. This study focuses on the following:

(1) deionized water droplets impinging on a polished surface at various surface temperatures resulting in single-phase (non-boiling) and two-phase (boiling) conditions,

(2) deionized water droplets impinging on a nanoporous structured surface for non-boiling and boiling surface temperatures, and

(3) water-based SWCNT nanofluid droplets impinging on a polished surface for non-boiling surface temperatures.

In addition, the disc surface temperature was also measured in separate experiments using a thin deposited gold layer on the polished silicon surface. The gold layer allows direct infrared imaging of the solid surface rather than the fluid. This method, along with detailed thermal results, are discussed in [35]. Results include the initial impact hydrodynamics, while looking at the ability of existing models to predict maximum spread distances. Also, the ability to predict the dynamic contact angle is presented along with some characteristics of the total evaporation process.
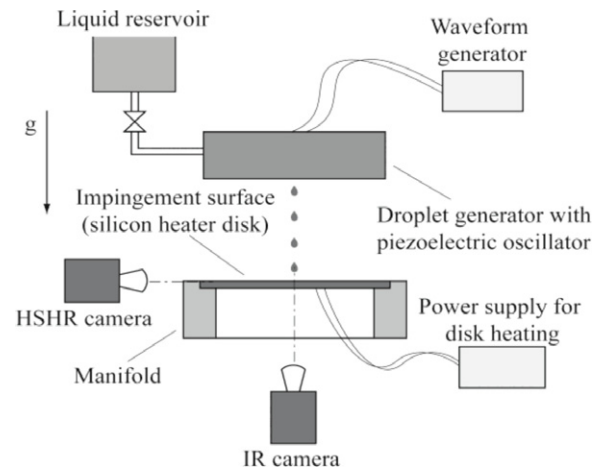

Figure 1. Sketch of the test facility.

2. Experimental set-up and data analysis

Distilled deionized water and nanofluid droplets impinging on solid surfaces were studied by recording the impingement process with a high speed camera at 7400 frames s^{-1}. A sketch of the experimental set-up is shown in figure 1. The components include the following: droplet generation system, impingement surface and heating system, imaging and lighting system. All components were synchronized so as to achieve simultaneous droplet imaging and thermal measurements.

The droplet generation system includes a Tektronix AWG 2021 Arbitrary Waveform Generator, a portable EL ageing driver sine wave I/O amplifier, a fluid reservoir and a piezoelectric driven droplet generator. The waveform generator produces a trigger to synchronize the droplet generator and camera. The droplet size and velocity at impingement were measured for a large number of samples to ensure repeatability. In this study, the impact drop diameter is 1.29 mm with a standard deviation of 0.03 mm for water and 1.18 mm with a standard deviation of 0.05 mm for the nanofluid. The impact velocity is 1.18 m s^{-1} with a standard deviation of 0.03 mm for water and 1.20 mm with a standard deviation of 0.04 mm for the nanofluid. The mean and standard deviation of droplet diameter and impact velocity for water and nanofluid is summarized and presented in table 1. The water droplet diameter is 8.5% larger than the nanofluid, and the water impact velocity is less than 1.7% different from that of the nanofluid.

Distilled deionized water and single-wall carbon-nanotube (SWCNT) nanofluid were used in the experiments to study the effect of nanoparticles on droplet impingement dynamics. The nanofluid is a water-based suspension with 0.2% by weight SWCNT and 0.5% by weight gum arabic. The range of diameters and lengths of the SWCNT is about 0.5–10 nm and 100–2000 nm, respectively. The nanofluid was prepared in a clean room following the procedure given in [36]. SWCNT and gum arabic powder were mixed in distilled deionized water. The mixture was then ultrasonicated for 3 h to obtain a stable nanoparticle suspension. Before each set of experiments the nanofluid was ultrasonicated for 3 h again to ensure full mixing
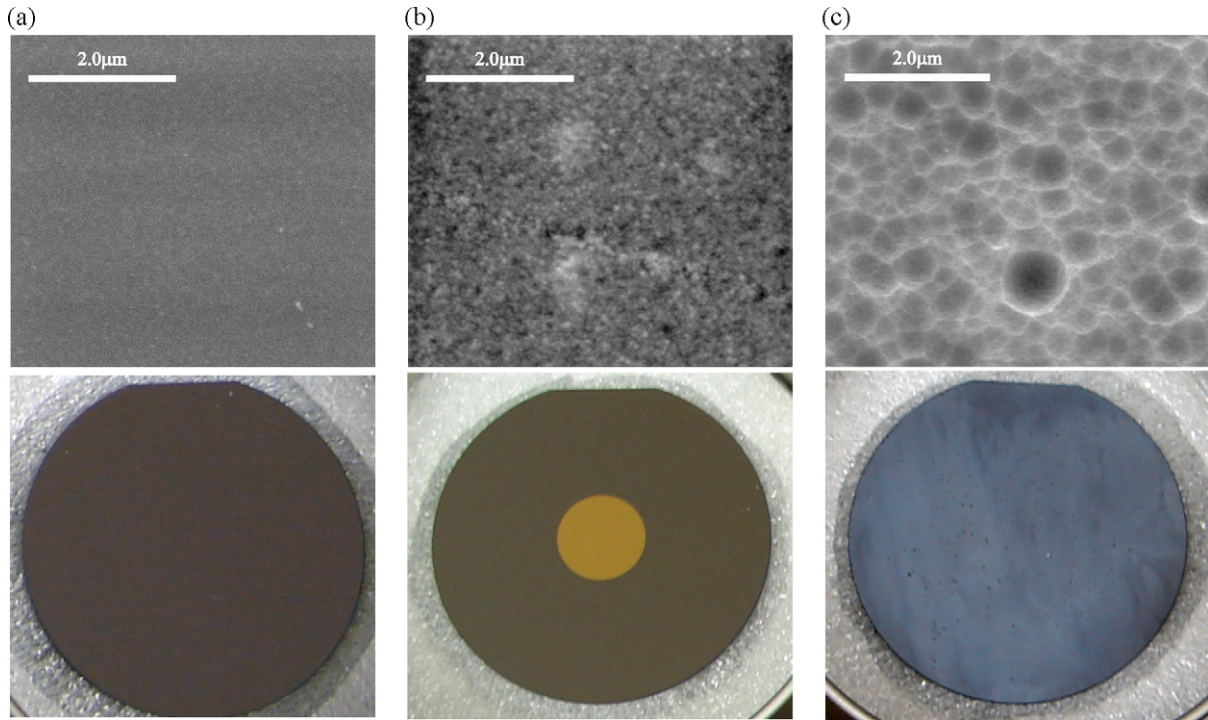
(a) (b) (c)

Figure 2. AFM images of the different test surfaces and photos of the actual discs: (a) polished silicon; (b) gold-coated silicon; (c) nanostructured porous silicon.

Table 1. Fluid properties at 25 °C and test conditions.

Fluid	d_o (mm)	v_o (m s^{-1})	Re_o	We_o	ρ (kg m^{-3})	μ (cp)	γ (dyne cm^{-1})
Water	1.29 ± 0.03	1.18 ± 0.03	1726	25.2	990.95	0.88	70.52
Nanofluid[a]	1.18 ± 0.05	1.20 ± 0.04	1615	23.3	996.77	1.195[b]	72.69

[a] Distilled deionized water with 0.2% by weight SWCNTs and 0.5% by weight gum arabic.
[b] Is measured from base fluid (distilled deionized water with 0.5% by weight gum arabic).

of the nanoparticles and base fluid. After each set of tests all the droplet delivery systems and surfaces were flushed and cleaned with distilled deionized water.

Three different impingement surfaces were used: a polished silicon, a thin gold-layer-coated silicon and a nanostructured silicon surface. Each impingement surface was a silicon disc with different surface treatment and was heated using thin film heaters underneath the disc. The silicon disc was 38 mm in diameter and 0.5 mm thickness. Images of the three surfaces and the impingement discs are shown in figure 2.

The imaging system includes a 10× micro-objective and a Phantom 5.0 high speed high resolution camera recording the dynamics of droplet impingement from a side view. The field of view of the 10× objective and adapter is approximately 5 mm square, with a resolution of 9 μm/pixel. The working distance was 3.5 cm. The pre-impact surface temperature was measured using the IR imaging system with a gold layer on the silicon and is also verified using two thermocouples placed in direct contact with the disc and covered with a thin layer of Ga–Sn to ensure an accurate surface temperature reading.

Density, viscosity and surface tension were measured for both water and the nanofluid. The measured density was 991 kg m^{-3} and 997 kg m^{-3} for water and the nanofluid,

respectively, with an uncertainty of less than 1%. Dynamic viscosity was measured using a Cambridge Viscosity Inc. ViscoLab 450 viscometer, with a accuracy ± 0.02 cp or $\pm 1.0\%$ of full range. The measured dynamic viscosity of water and base fluid of the nanofluid at room temperature (25 °C) was 0.88 cp and 1.195 cp, respectively. The pendant drop method was used to determine the surface tension. Details of the pendant drop method can be found in [37–40]. The measured surface tension of water and nanofluid were 70.52 and 72.69 dyne cm^{-1}, respectively. Fluids property measurement results are summarized in table 1 where the data were taken at room temperature, nominally 25 °C. The water and nanofluid are very similar in density and surface tension, but have a 37% difference in dynamic viscosity. The wettability of the fluids and surface combinations is given in table 2 in terms of the equilibrium contact angle at room temperature conditions. Water on the nanostructured surface has a significantly larger contact angle (more wetting) than for the polished surface. Similarly the nanofluid contact angle increases for the gold surface, but is less than that for water on the polished surface.

Surface heating conditions are summarized in table 3 where P_{tot} is the total power in watts applied to the heater

Table 2. Wettability of water and nanofluids on the various surfaces.

	$\theta_{\text{eq}-\text{NH}}$ (at 25 °C) (deg)
Water on polished surface (w–p)	46
Water on gold surface (w–g)	58
Water on nanostructured surface (w–ns)	65
Nanofluid on polished surface (nf–p)	32
Nanofluid on gold surface (nf–g)	54

Table 3. Pre-impact surface temperature summary.

	Non-boiling				Boiling		
	$T0$	$T1$	$T2$	$T3$	$T4$	$T5$	$T6$
P_{tot} (W)	0	1.8	3.1	4.3	5.1	5.4	5.7
$T_{\text{s},o}$ (°C)	25	68.9	87.1	111.7	146.1	153.4	185.0

rings and $T_{\text{s},o}$ is the surface temperature before droplet impact. The seven surface temperatures correspond to one of three conditions: a non-heating (room temperature) case, three non-boiling cases and three boiling cases.

The molecular-kinetic theory's dynamic contact angle model is evaluated by comparing the experimental data with the prediction of dynamic contact angle as a function of contact line velocity. The M-K model is based on molecular displacement theory; the contact line velocity can be expressed as equation (1):

$$v_{\text{cl}} = 2k_{\text{w}}^o \sinh \left\{ \frac{\sigma \lambda^2}{2k_{\text{B}} T} (\cos \theta_{\text{E}} - \cos \theta) \right\} \quad (1)$$

where v_{cl} is contact line velocity, k_{w}^o is the frequency of the molecular displacement, λ is the average molecular path distance, k_{B} is the Boltzmann constant, T is absolute temperature in kelvin, θ_{E} is the equilibrium contact angle and θ is the dynamic contact angle.

Four models used to predict maximum spreading diameter are evaluated in this study. These models are based on energy analysis of a droplet before impact and at maximum spreading. The energy prior to impact includes the kinetic energy and droplet–surface energy. At droplet maximum spread the kinetic energy is taken as zero, due to zero velocity and only consists of the surface energy, with the drop approximated as a flat disc. During spreading energy is dissipated by viscous action with the surface. The basic energy balance can be expressed in non-dimensional form, with $Re = \frac{\rho v_o d_o}{\mu}$, $We = \frac{\rho v_o^2 d_o}{\sigma_{\text{LV}}}$ and $d_{\text{max}}^* = \frac{d_{\text{max}}}{d_o}$ by equating the sum of the initial kinetic and surface energies to the final energy less the energy dissipated W_{diss} as, see [5] or [20]:

$$\frac{W_{\text{diss}}}{\pi d_o^2 \sigma_{\text{LV}}} = \left(\frac{We}{12} + 1 \right) - \frac{2}{3 d_{\text{max}}^*} - \frac{1}{4} (1 - \cos \theta_o) d_{\text{max}}^{*2} \quad (2)$$

where ρ is the density, σ_{LV} is the liquid vapor surface tension, d_o is the droplet diameter prior to impact and d_{max} is the maximum spreading diameter.

The four models used to predict maximum spreading use different approximations to arrive at an expression for the total dissipation by viscous forces, W_{diss}. The models estimate this assuming a velocity gradient at the surface valid over the entire

Table 4. Model comparison of dissipation terms for maximum spreading diameter prediction.

Model	$\dfrac{W_{\text{diss}}}{\pi d_o^2 \sigma_{\text{LV}}}$
Chandra	$\dfrac{3We}{8Re}\beta^4$
P–F	$\dfrac{We}{3\sqrt{Re}}\beta^2$
Mao	$0.2\dfrac{We^{0.83}}{Re^{0.33}}\beta^2$
Liu	$0.0018\dfrac{We}{\sqrt{Re}}\left[1 + 27.3\left(\dfrac{Ra}{d_o}\right)^{0.76}\right]\beta^4$
	Ra is the surface roughness

contact region. The Chandra model simplifies the estimation by scaling the velocity gradient with the impact velocity and the droplet height when the drop reaches maximum diameter. The P–F model estimates the dissipation energy within a thin boundary layer based on laminar boundary layer growth. The Mao model again uses a thin laminar boundary layer for scaling, but introduces empirical coefficients. Finally, the Liu model treats the droplet spreading as a stagnation point flow and expresses dissipation energy due to friction, while also considering the influence of surface roughness. Table 4 shows the dissipation term estimation for each of the four models. For the Liu model a set of coefficients are also developed based on the current experimental data.

The data used to evaluate the models were obtained using the image data by applying the Prewitt method of edge detection, which is based on a maximum gradient method, as shown in figure 3. The method was used to determine the droplet diameter, impact velocity, impact time, spreading diameter, spreading velocity, spreading height and contact angle, as illustrated in figure 3(b). Figure 3(a) shows images of the droplet during the initial impact. The first image shows the droplet just prior to impact. From the frames prior to impact, the droplet diameter (d_o) and impact velocity (v_o) were measured. The time is determined to be zero at the moment of impact and the spreading time can be calculated relative to the impact time.

3. Results

3.1. Impingement process

As reported in [35] and elsewhere, distinct stages are observed during impingement. In this case of non-splashing with heat transfer the stages are: initial impact (with a large temperature transient), boiling (if the surface temperature is high enough), evaporation (with near-constant wetting diameter and temperature), evaporation (with a receding contact line) and final dry-out. Images of a typical impingement with boiling are shown in figure 4, where (a)–(e) are the images corresponding to the five stages listed. During initial impact, the droplet rapidly spreads, rebounds and then oscillates at a near-constant wetting diameter. Boiling involves initial nucleation followed by severe boiling including
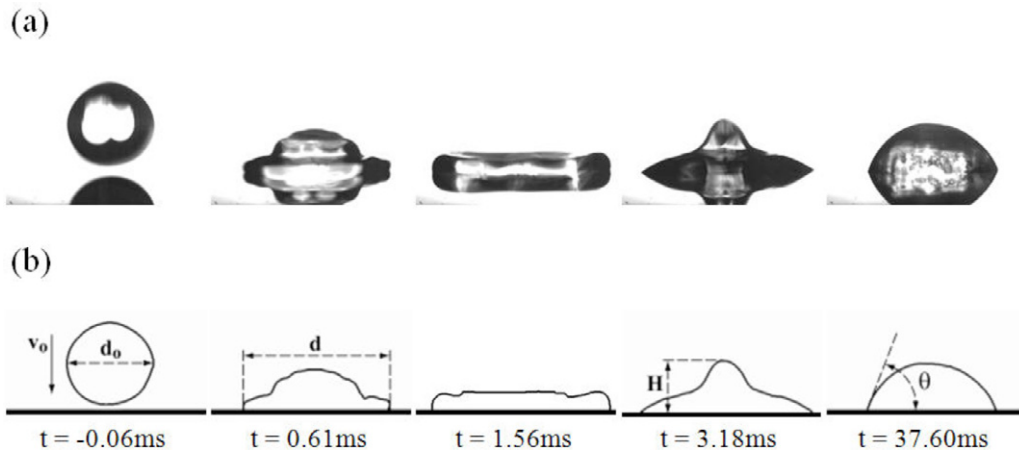
Figure 3. Image processing illustration: (a) raw images; (b) images of edge detection and parameter measurement illustration.
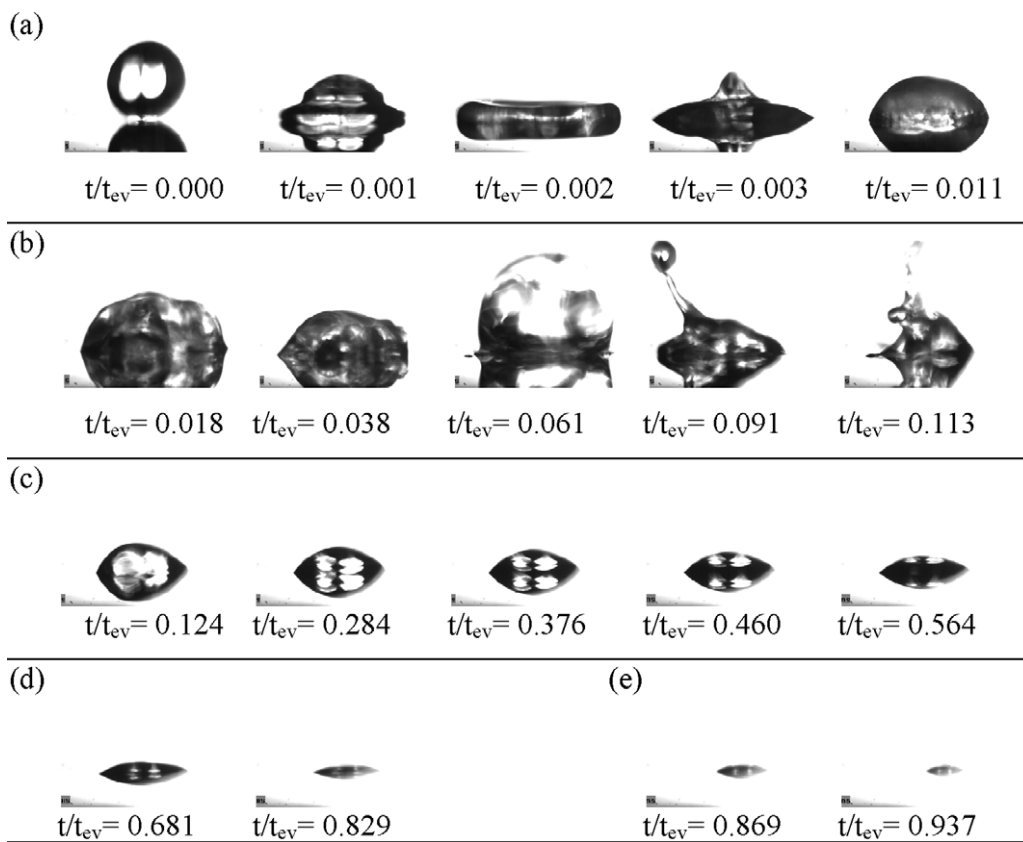

Figure 4. Droplet images of the five stages of impingement process for water impinging on polished surface at $T_{s,o} = 185\,°C$: (a) initial impact, (b) boiling, (c) near-constant wetting diameter evaporation, (d) fast receding contact line evaporation, (e) final dry-out.

droplet ejection and expansion, and evaporative cooling with the absence of boiling. At non-boiling heating levels the droplet experiences evaporation once the oscillation period ends. Droplet height decreases while the wetting diameter remains nearly constant. When a critical angle is reached, the droplet diameter diminishes rapidly and then dry-out occurs. Figure 5 shows the spreading diameter evolution during impingement at a surface temperature of 153 °C, using water droplets impinging on a polished surface as an example. The droplet diameter is non-dimensionalized by the pre-impact

diameter, $d^* = d/d_o$. The five stages are marked in the figure as A–E. Stage A, initial impact, takes place in less than 1% of the total impingement time. The details of this stage are presented later. Stage B, boiling, lasts about 10%–15% of the total time to full evaporation. During this stage, the droplet wetting diameter has great variations due to droplet ejection and expansion. Stage C, near-constant wetting diameter evaporation, has the droplet wetting diameter nearly constant while droplet height and contact angle decrease. This stage lasts about 60% of the total evaporation time and is followed by
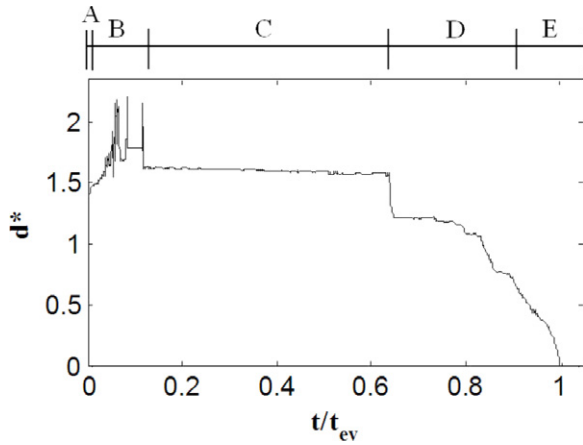
Figure 5. Non-dimensional spreading diameter (d^*) as a function of scaled non-dimensional time (t/t_{ev}): illustration of the five stages of impingement process for water impinging on polished surface at $T_{s,o} = 153\,°C$: (A) initial impact, (B) boiling, (C) near-constant wetting diameter evaporation, (D) fast receding contact line evaporation, (E) final dry-out.

stages D and E, fast receding contact line evaporation and final dry-out. These two stages occur very rapidly compared to stage C. In figure 5, at the beginning of stage D, the wetting diameter jumps then stays constant again during stage D before the rapid decrease. During stage C, the contact angle decreases due to mass loss during evaporation. When a critical contact angle is reached, the droplet is observed to make a near-instantaneous jump to a smaller contact area with the surface, resulting in a higher contact angle and higher droplet height. A possible explanation is that, when the contact angle reaches a critical value, the component of the surface tension force along the surface at the three-phase interface becomes large enough to nearly instantaneously reduce the diameter which results in a greater contact angle and stable configuration. Once this occurs the droplet continues to evaporate, again decreasing the contact angle. A series of discrete critical angles may occur with the corresponding instantaneous jump to smaller diameters. Eventually total dry-out occurs. The critical contact angle, for all surfaces, was measured just prior to this rapid jump and for all pre-impact surface temperatures and all three surfaces. The critical contact angle is found to be remarkably constant at approximately 10°.

Figure 6 compares the droplet diameter evolution for six different surface temperatures corresponding to non-boiling and boiling conditions for water droplets impinging on the nanostructured surface. It shows the droplet spreading diameter as a function of time. Note here that the time is non-dimensionalized by the total evaporation time, so as to compare the spreading stages at different surface temperature conditions, since the total evaporation times are greatly different for different surface temperature conditions. The total time for evaporation, shown in table 5, ranges from 1.3 to 53.2 s, for surface temperatures ranging from 68.9 to 185 °C. Figure 6(a) is for non-boiling conditions and (b) is for boiling conditions. When non-boiling, the droplet spreads further after initial impact compared to that for boiling conditions. The droplet spreading diameter starts decreasing earlier in the
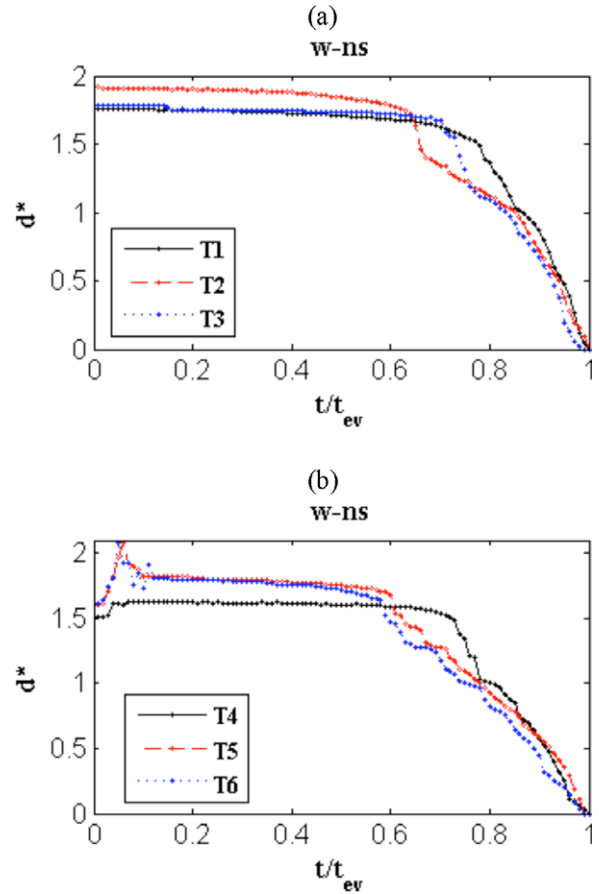

Figure 6. Impingement process non-dimensional spreading diameter (d^*) as a function of non-dimensional time (t^*) for water impinging on the nanostructured surface at six pre-impact surface temperatures: (a) non-boiling: $T1 = 68.9\,°C$, $T2 = 87.1\,°C$, $T3 = 111.7\,°C$; (b) boiling: $T4 = 146.1\,°C$, $T5 = 153.4\,°C$, $T6 = 185.0\,°C$.

Table 5. Evaporation time versus surface temperature for: water on the polished surface (w–p), water on the nanostructured surface (w–ns) and nanofluid on the polished surface (nf–p).

$T_{s,o}$ (°C)	68.9	87.1	111.7	146.1	153.4	185.0
$t_{ev,w-p}$ (s)	53.2	16.0	6.1	3.1	2.4	1.3
$t_{ev,w-ns}$ (s)	37.7	13.6	5.0	3.0	2.1	1.7
$t_{ev,nf-p}$ (s)	25.0	11.7	3.8	—	—	—

boiling condition than the non-boiling condition. These trends are observed in the cases of water impinging on all three surfaces.

The total normalized evaporation times (normalized by d_o/v_o) as a function of surface temperature are presented in figure 7. The total evaporation time of water impinging on the polished surface, water impinging on the nanostructured surface and the nanofluid impinging on the polished surface are compared. The evaporation times for the nanofluid and nanostructured surface are consistently lower than those for the polished surface. The evaporation time difference is most pronounced at the lower surface temperatures, which are the non-boiling cases. Evaluating all cases it is found that the decrease of the total evaporation time for the nanostructured surface remains at about 20% for both the non-boiling and
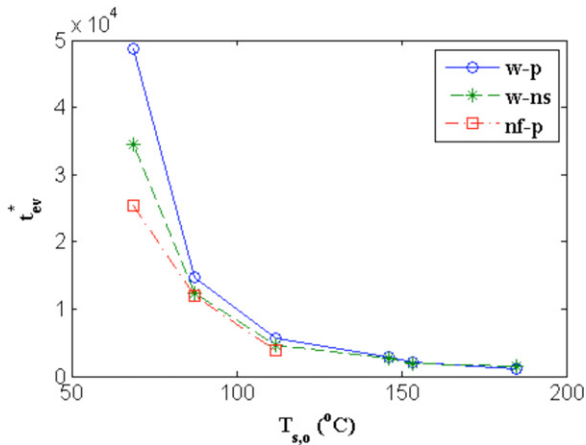
Figure 7. Non-dimensional evaporation time (t_{ev}^*) as a function of pre-impact surface temperature ($T_{s,o}$) for three cases: water on polished surface, water on nanostructured surface and nanofluid on polished surface.

boiling cases and 37% for the nanofluid in non-boiling cases. The decrease of the total evaporation time is believed to be a consequence of the increased spreading diameter for both nanofluid and nanostructured heated cases. For the same droplet size and velocity, this result may have consequences in improving spray cooling applications. However, data needs to be extended to a large range of nanofluids and nanostructured surfaces looking at relevant effects of size scales and surface characteristics.

3.2. Initial impact stage

During the entire impingement process the droplet goes through impact, advancing, maximum spreading, receding and a period of oscillation with pinned contact line. For the non-heating case once the oscillations diminish the drop comes into equilibrium at a contact angle denoted as θ_{eq-NH}. Figure 8 shows droplet images at typical moments during the initial impact stage. Figure 9 illustrates the normalized spreading parameters as a function of time for a typical non-boiling case. All variables are normalized by the pre-impact values. The non-dimensional parameters include spreading diameter, spreading velocity, droplet height and dynamic contact angle. Figure 9(a) shows a rapid initial advancing to a maximum diameter followed by a rebound. The maximum spreading for all cases occurs within $t^* < 2$ and the initial rebound occurs within $t^* < 5$. In figure 9(b), the spreading velocity shows an

inverse relationship to the spreading diameter, with a maximum value right after impact, then reaches zero when the spreading diameter is at its maximum. Figures 9(c) and (d) show that the droplet height and contact angle are at essentially the same phase oscillating, where a higher droplet height results in larger contact angles. These are shown to illustrate the oscillatory behavior of the droplets even after the contact line has come to rest, as shown in figure 9(a).

The effect of using a nanostructured surface is evaluated by comparing the results of water droplets impinging on three different surfaces: polished silicon, gold-coated silicon and a nanostructured silicon at both non-boiling and boiling conditions. The comparison of spreading diameter, droplet height and dynamic contact angle are shown in figures 10–12. Results at three surface temperatures corresponding to non-heating ($T0$), non-boiling ($T2$) and boiling ($T5$) conditions are presented. These results are averages over typically ten runs. Water droplets impinging on a polished surface are used as a reference case.

Figure 10 shows representative non-dimensional time traces of the droplet spreading diameter for non-heating, non-boiling and boiling cases. For non-heating conditions, in figure 10(a), the initial spreading is not significantly affected by the different surfaces. However, the equilibrium spreading diameter is different, with the largest occurring for the polished surface. The reduction in spreading for the gold and nanostructured surfaces is consistent with the observed increase in droplet height for these cases as shown in figure 11(a). In figure 10(b), the non-boiling heated cases show a reduction in spreading for the polished and gold surfaces while the nanostructured surface shows an increase. In figure 10(c), for the boiling cases all equilibrium spreading diameters are shown to be reduced, with the nanostructured spreading diameter the largest for these cases. The increased spreading over the nanostructured surface suggests a greater potential for increased surface transport.

The corresponding change in droplet height during initial impact is shown in figure 11. The initial spreading and rebound is similar for all cases. The subsequent oscillations all seem to exhibit approximately the same phase and amplitude. The boiling cases show increased heights, consistent with the observed reduction in spreading diameter shown in figure 10(c). As would be expected there is little effect of the surface on the droplet height dynamics.

The time traces of the normalized dynamic contact angle, θ^* (normalized by the equilibrium value for non-heating conditions) are shown in figure 12. The time responses

(a)	(b)	(c)	(d)	(e)

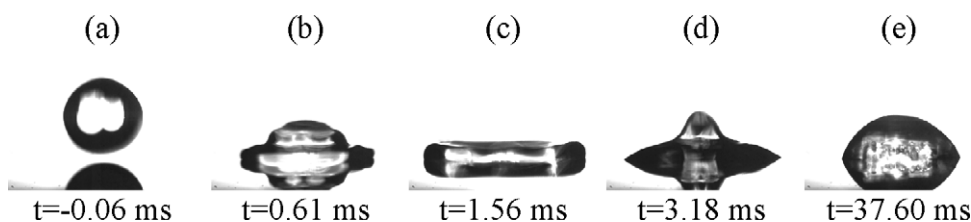| t=-0.06 ms | t=0.61 ms | t=1.56 ms | t=3.18 ms | t=37.60 ms |

Figure 8. Typical moments of droplet initial impact stage: (a) before impact, (b) advancing, (c) maximum spreading, (d) receding, (e) oscillating.
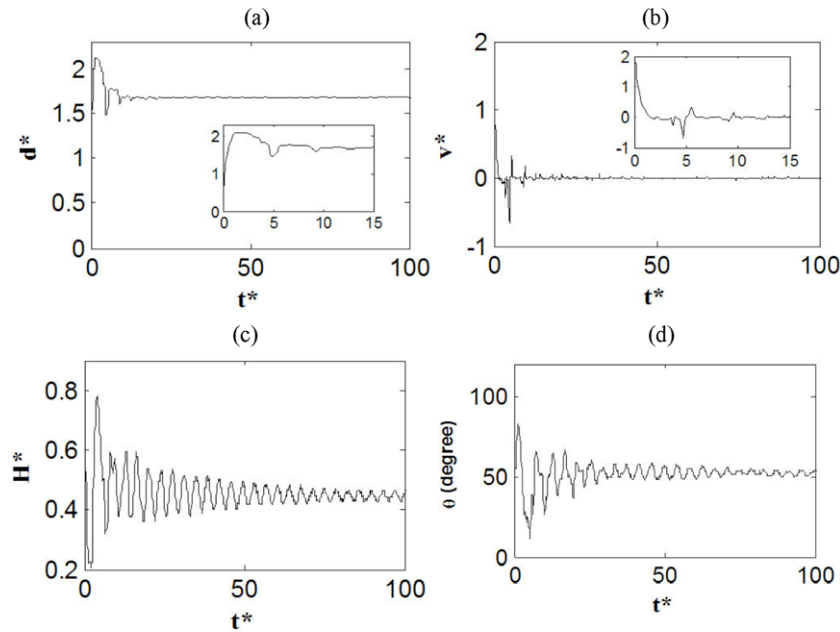
Figure 9. Initial impact non-dimensional parameter time evolution illustration at T $_{s,o}$ = 87 °C: (a) d^* versus t^*, (b) v^* versus t^*, (c) H^* versus t^*, (d) θ^* versus t^*.

are similar: however, the gold and nanostructured surfaces show a reduction of the initial relative advancing contact angle. This difference is larger for the heated cases, with differences extending over the entire oscillatory period of the initial impact stage when the surface is heated. These results indicate that the surface energy differences are enhanced somewhat for the nanostructured surface with a reduction of the relative advancing and receding contact angles during the initial impact. Also, the contact angle oscillations that occur once spreading has come to equilibrium seem to be damped.

Based on these results it is seen that the initial spreading, consisting of a moving contact line, is essentially complete beyond $t^* = 5$ for all surfaces. However, oscillations and resultant internal motion persist well beyond this, $t^* > 20$. During the initial spreading time, the droplet is experiencing an initial rapid temperature rise while the surface temperature is dropping. However, the bulk of the heat transfer occurs after the droplet has reached an equilibrium diameter [35].

Similarly, the effect of using the nanofluid is evaluated by comparing the results of the nanofluid droplet impinging on a polished surface and a gold-coated surface with water droplets impinging on a polished surface for non-boiling conditions. Here the case of water impinging on a polished surface serves as a reference case. The droplet spreading diameter, droplet height and dynamic contact angle comparison are shown in figures 13–15, respectively, for surface temperatures in a non-heating ($T0$) and non-boiling ($T2$) condition.

For non-heating conditions, figure 13(a), the nanofluid impingement shows a similar trend to water: the initial spreading is complete within $t^* < 5$ and the oscillation of droplet height and contact angle continues beyond $t^* > 20$. The spreading diameter for all three cases shows little difference, with the nanofluid equilibrium diameter a little larger than that of water impinging on a polished

surface. However, for the non-boiling condition, figure 13(b), with a higher surface temperature, the spreading diameter of the nanofluid increases significantly while that of water decreases somewhat. Both maximum spreading diameter and equilibrium diameter are much larger for $T2 = 87.1$ °C than for the non-heating condition. Correspondingly, as shown in figures 14 and 15, the droplet height and equilibrium contact angle decrease significantly for $T2 = 87.1$ °C compared with $T0 = 25$ °C, due to the increase of droplet spreading diameter, for a given droplet volume. The results indicate that the nanofluid spreads much further than water as the surface temperature increases, which results in a larger contact area, and therefore the shorter total evaporation time and enhanced heat transfer eventually. This is consistent with the greater wettability of the fluid at room temperature.

During spreading the molecular-kinetic theory's (M-K) dynamic contact angle model was evaluated by comparing the experimental data with the prediction of dynamic contact angle as a function of contact line velocity. The parameters used in the model were not adjusted for each different case and are based on the result of the experimental and numerical study of Sangplung and Liburdy [4]; the values used are $\kappa_w = 4.62 \times 10^7$ s^{-1} and $\lambda = 6.25 \times 10^{-10}$ m. These values are consistent with those given in [19] for a range of liquids and solid surfaces. Figure 16 shows the comparison of experimental data (water impinging on a polished surface) with the M-K model prediction at three different surface temperatures, corresponding to non-heating, non-boiling and boiling conditions. Droplet spreading velocities are high for $t^* < 5$ right after initial impact, then decrease rapidly during oscillations as shown in figure 9(b). Hence most velocity data are at the lower range ($v^* < 0.1$). Results show that the M-K model agrees well with current experimental data for the low velocity range (less than 0.1), but largely over-predicts
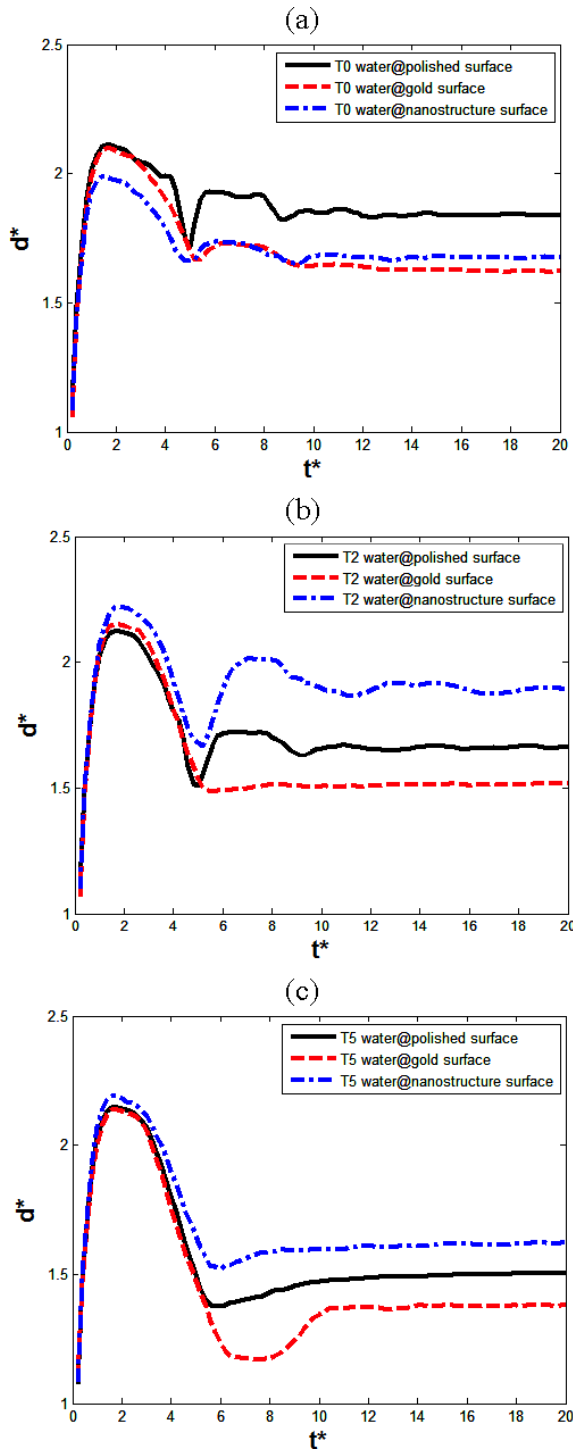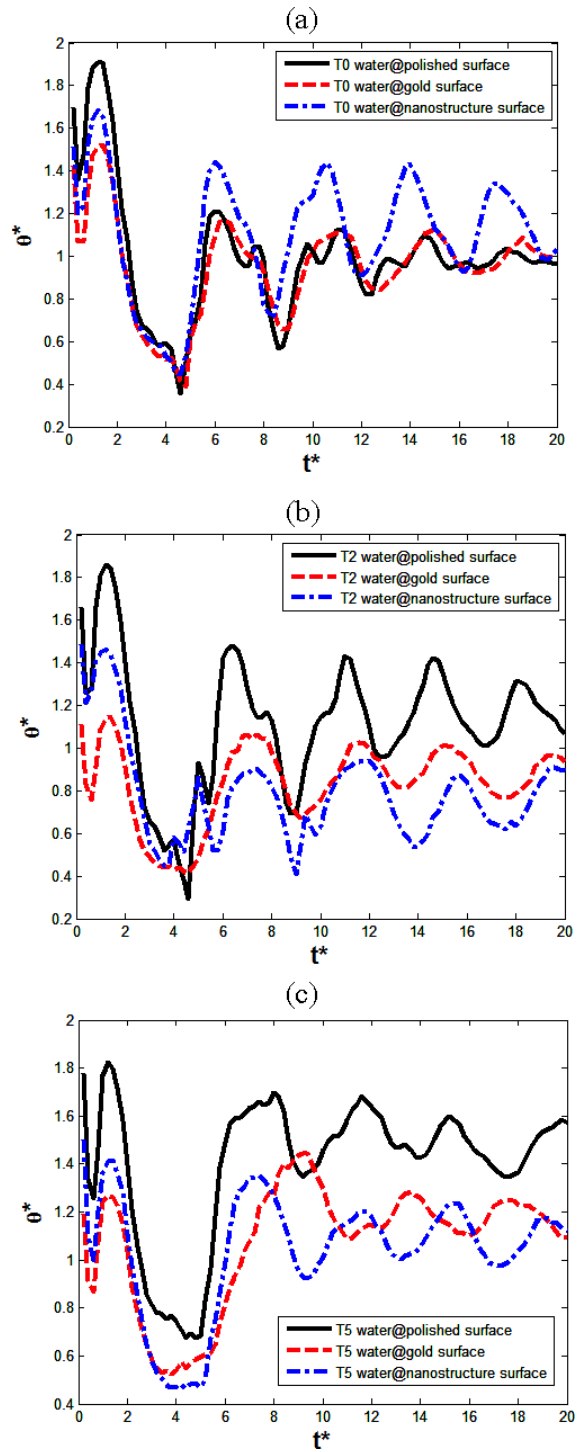
Figure 10. Initial impact: non-dimensional spreading diameter (d^*) as a function of non-dimensional time (t^*) for water droplets impinging on three surfaces (polished, gold-coated and nanostructured porous surfaces), (a) non-heating, $T0 = 25\,°C$; (b) non-boiling $T2 = 87.1\,°C$; (c) boiling $T5 = 153.4\,°C$.

Figure 11. Initial impact: non-dimensional droplet height (H^*) as a function of non-dimensional time (t^*) for water droplets impinging on three surfaces (polished, gold-coated and nanostructured porous surfaces), (a) non-heating, $T0 = 25\,°C$; (b) non-boiling $T2 = 87.1\,°C$; (c) boiling $T5 = 153.4\,°C$.

the dynamic contact angle at higher velocities (which occur right after initial impact). The trend of the data shows that at the higher velocities the dynamic contact angle actually decreases. This decrease is shown to occur for non-wetting, high momentum drops [19]. However, here it is shown for

partially wetting drops. This is mostly likely a consequence of the complex flow pattern within the drop during impact at high inertia where there is a rapid change in fluid momentum (direction and magnitude). Also a thin precursor film most likely has not developed at this point, altering the contact line
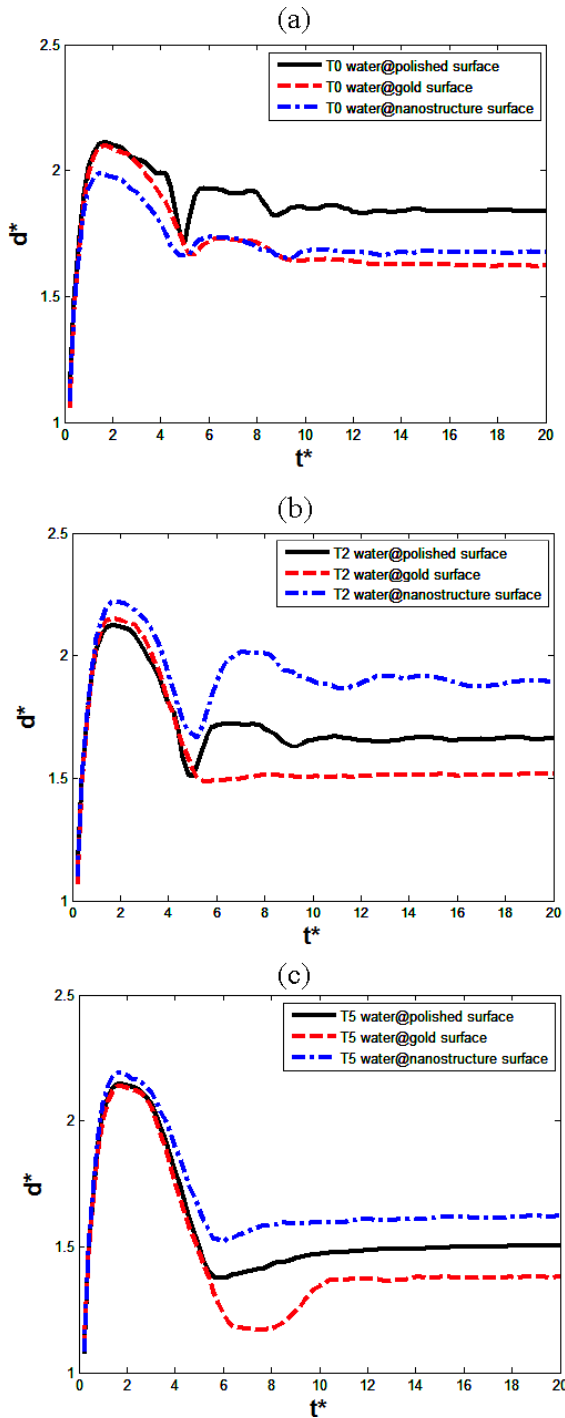
Figure 12. Initial impact: non-dimensional dynamic contact angle (θ^*) as a function of non-dimensional time (t^*) for water droplets impinging on three surfaces (polished, gold-coated and nanostructured porous surfaces): (a) non-heating, $T0 = 25\,°C$; (b) non-boiling $T2 = 87.1\,°C$; (c) boiling $T5 = 153.4\,°C$.

Figure 13. Initial impact: non-dimensional droplet spreading diameter (d^*) as a function of non-dimensional time (t^*) at: (a) non-heating $T0 = 25\,°C$; (b) non-boiling $T2 = 87.1\,°C$ for three cases (nanofluid on polished and gold-coated surfaces and water on polished surface).

region characteristics and relevant force relationship such as inertia, gravitational and surface tension during this portion of the flow. Bayer and Megaridis [19] provide extensive comparisons with the M-K model showing variations in first and second cycle results, attributed to a possible thin liquid film developing after the first cycle. They also found that the
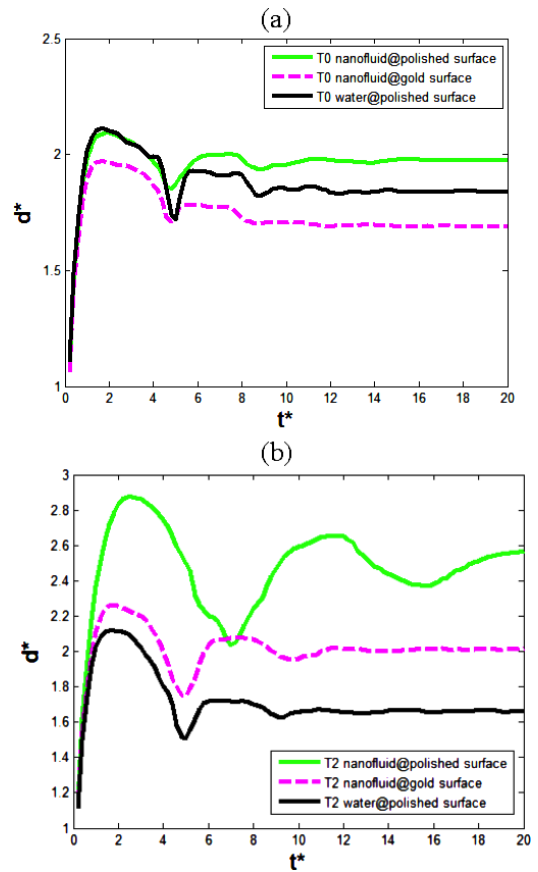
partially wetting and wetting cases yielded better consistency with the model than the non-wetting case. The partially wettable surface results of [19] do show a slight overshoot as seen in figure 16 but it is not as pronounced. This may be a result of a higher inertia at impact in the present case.

Maximum spreading diameter at initial impact is one of the important parameters to characterize droplet impingement dynamics and subsequent heat transfer. The maximum diameter typically occurs within $t^* < 2$. The results of the predictions using the four models based on surface energy analysis, described previously, are compared with current experimental data in figure 17. The designation 'Liu empirical' uses Liu's model with the empirical coefficients obtained from data in the current study. It should be noted that Liu's data was at significantly larger Reynolds numbers (9200–26 500) and Weber number (258–1670) than the current data by approximately an order of magnitude. Results show that the four non-dimensional maximum spreading diameter predictions all significantly over-predict the results. This over-prediction is due to the relative under-estimation of the dissipation energy during the impinging process. By adjusting Liu's model using the data from this study the predictions can be made to match experimental results, but this is merely force-fitting the data. For the conditions studied these models fail to
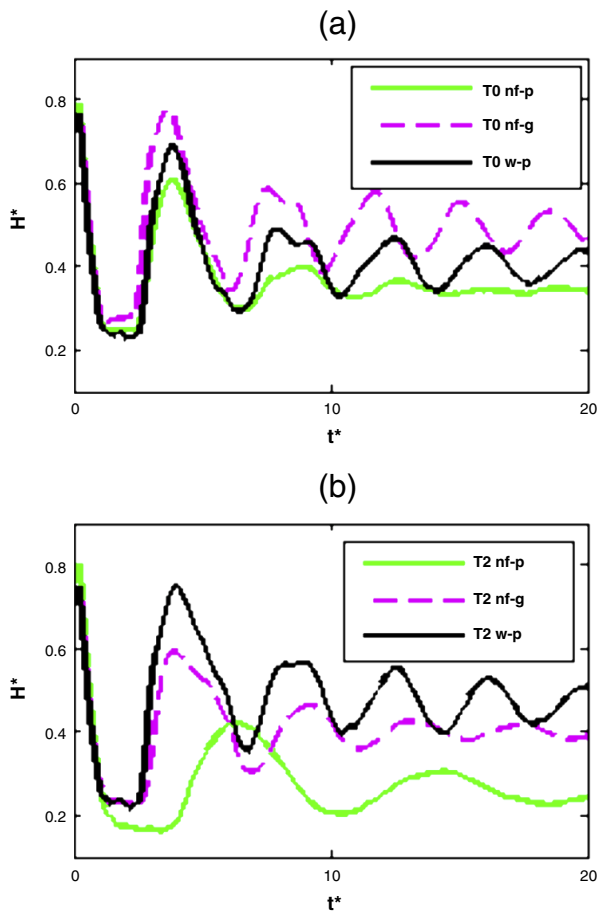
Figure 14. Initial impact: non-dimensional droplet height (H^*) as a function of non-dimensional time (t^*) at: (a) non-heating $T0 = 25\,°C$; (b) non-boiling $T2 = 87.1\,°C$ for three cases (nanofluid on polished and gold-coated surfaces and water on polished surface).
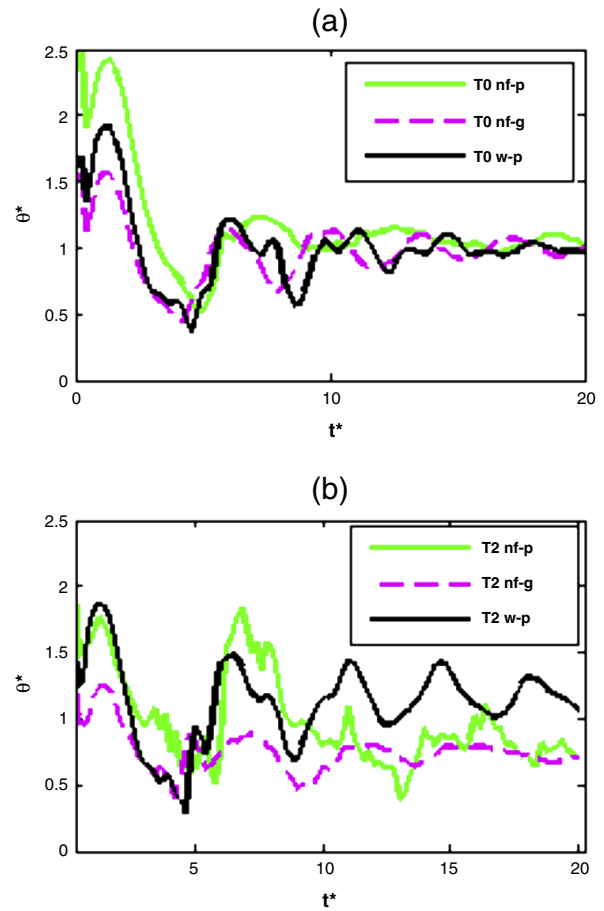

Figure 15. Initial impact: non-dimensional dynamic contact angle (θ^*) as a function of non-dimensional time (t^*) for: (a) non-heating $T0 = 25\,°C$; (b) non-boiling $T2 = 87.1\,°C$ for three cases (nanofluid on polished and gold-coated surfaces and water on polished surface).

predict spreading and a more universal relationship needs to be found to properly predict the maximum spreading diameter. Consequently, models based on more realistic dissipation estimates such as by Roisman *et al* [24] may be required.

4. Conclusions

This study investigates the hydrodynamic characteristics of droplets impinging on heated surfaces using high speed imaging and evaluates the effect of surface temperature for water and a nanofluid on both polished and nanostructured surfaces. Droplet impingement behavior is summarized in terms of the observation of five stages: initial impact, boiling (if the surface temperature is high enough), near-constant wetting diameter evaporation, fast receding contact line evaporation and final dry-out. Initial impact occurs within approximately $t^* < 5$. At lower heating levels the droplet experiences evaporation once the oscillation period ends, with a constant diameter evaporation during approximately 60% of the total time. A critical angle was measured to be near 10° when the droplet suddenly retracts to a lower contact area. The critical angle does not change significantly with either temperature or surface. Results show that the nanofluid causes
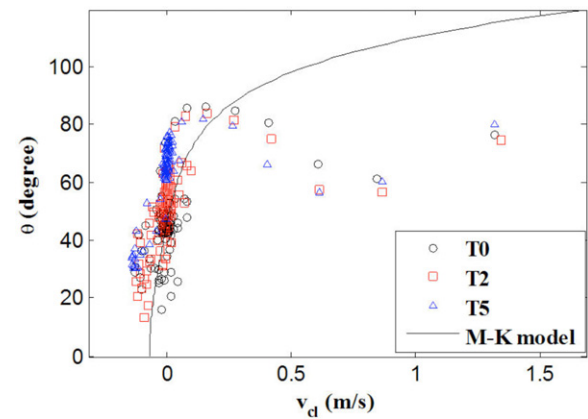

Figure 16. Dynamic contact angle (θ) as a function of contact line velocity (v_{cl}), comparison of experiment data and M-K model prediction for water impinging on polished surface at three surface temperatures: non-heating $T0 = 25\,°C$, non-boiling $T2 = 87.1\,°C$ and boiling $T5 = 153.4\,°C$.

larger spreading diameters and a decrease in equilibrium contact angle with increasing temperature; this despite the non-heated contact angle being less than that of water on
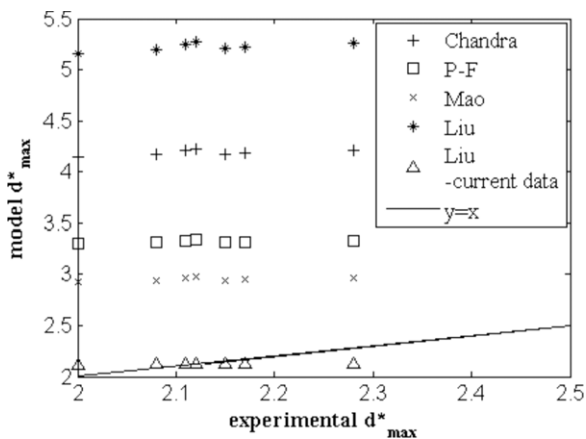
Figure 17. Comparison of maximum spreading diameter models' prediction versus experimental d^*_{max} for water impinging on a polished surface at non-heating $T_{s,o} = 25\,^{\circ}\mathrm{C}$.

the polished surface. Both nanofluid and nanostructured surfaces are found to enhance the heat transfer for evaporative cooling at lower power levels, which is indicated by a shorter evaporation time. The total droplet evaporation time is found to be reduced by approximately 20% and 37%, using the nanostructured surface and nanofluid, respectively, compared with the polished surface. The dissipation models show poor agreement with the maximum spreading for the low Reynolds number and Weber numbers studied, most likely indicating stronger viscous and surface tension effects, requiring more exact representation of the energy dissipation during initial spreading.

References

[1] Moita A S and Moreira A L 2002 The dynamic behavior of single droplets impacting onto a flat surface *ILASS-Europe 2002 (Zaragoza, Sept.)*

[2] Chow C K and Attinger D 2003 Visualization and measurements of microdroplet impact dynamics on a curved substrate *Proc. FEDSM'03: 4th ASME-JSME Joint Fluids Engineering Conf.*

[3] Cossali G E and Brunello G 1999 Impact of a single drop on a liquid film: experimental analysis and comparison with empirical models *Italian Congr. Thermofluid Dynamics UIT (Ferrara)*

[4] Sangplung S and Liburdy J A 2007 Effect of dynamic constant angle on single/successive droplet impingement *IMECE 2007-41603: Proc. ASME IMECE 2007 (Seattle, WA)*

[5] Liu J, Franco W and Aguilar G 2008 Effect of surface roughness on single cryogen droplet spreading *J. Fluids Eng.* **130** 041402

[6] Bernardin J D, Mudawar I, Walsh C B and Franses E I 1997 Contact angle temperature dependence for water droplets on practical aluminum surfaces *Int. J. Heat Mass Transfer* **40** 1017–33

[7] Rymkiewicz J and Zapalowicz Z 1993 Analysis of the evaporation process for water droplet on flat heated surface *Int. Commun. Heat Mass Transfer* **20** 687–97

[8] Hu H and Larson R 2002 Evaporation of a sessile droplet on a substrate *J. Phys. Chem.* B **106** 1334–44

[9] Bhardwaj R and Attinger D 2007 A numerical model for the evaporation of a nanoliter droplet on a solid, heated substrate *IMECE2007-43088: Proc. IMECE2007 (Seattle, WA)*

[10] Rioboo M, Marengo M and Tropea C 2002 Time evolution of liquid drop impact onto solid, dry surfaces *Exp. Fluids* **33** 112–24

[11] Sikalo S and Ganic E N 2006 Phenomena of droplet–surface interactions *Exp. Therm. Fluid Sci.* **31** 97–110

[12] Shen J, Liburdy J A, Pence D V and Narayanan V 2008 Single droplet impingement: effect of nanoparticles *FEDSM2008-55192: Proc. ASME Fluids Engineering Conf.*

[13] Jai W and Qiu H-H 2003 Experimental investigation of droplet dynamics and heat transfer in spray cooling *Exp. Therm. Fluid Sci.* **27** 829–38

[14] Chandra S, di Marzo M, Qiao Y M and Tartarini P 1996 Effect of liquid–solid contact angle on droplet evaporation *Fire Saf. J.* **27** 141–58

[15] Dunn G J, Wilson S K, Duffy B R and Sefiane K 2009 Evaporation of a thin droplet on a thin substrate with a high thermal resistance *Phys. Fluids* **21** 052101

[16] Hoffman R L 1975 A study of the advancing interface *J. Colloid Interface Sci.* **50** 228–41

[17] Cox R G 1998 Inertial and viscous effects on dynamic contact angles *J. Fluid Mech.* **357** 249–78

[18] Blake T D and Haynes J M 1969 Kinetics of liquid displacement *J. Colloid Interface Sci.* **30** 421–3

[19] Bayer I S and Megaridis C M 2006 Contact angle dynamics of droplets impacting on flat surfaces with different wetting characteristics' *J. Fluid Mech.* **558** 415–49

[20] Chandra S and Avedisian C T 1991 On the collision of a droplet with a solid-surface *Proc. R. Soc.* A **432** 13–41

[21] Pasandideh-Fard M, Qiao Y M, Chandra S and Mostaghimi J 1996 Capillary effects during droplet impact on a solid surface *Phys. Fluids* **83** 650–9

[22] Mao T and Kuhn D 1997 Spread and rebound of liquid droplets upon impact on flat surfaces *AIChE J.* **439** 2169–79

[23] Yarin A L 2006 Drop impact dynamics: splashing, spreading receding, bouncing *Annu. Rev. Fluid Mech.* **38** 159

[24] Roisman I V, Beberovic E and Tropea C 2009 Inertia dominated drop collisions. I. On the universal flow in the lamella *Phys. Fluids* **21** 052103

[25] Silk E A, Kim J and Kiger K 2006 Spray cooling of enhanced surfaces: impact of structured surface geometry and spray axis inclination *Int. J. Heat Mass Transfer* **49** 4910–20

[26] Silk E A, Kim J and Kiger K 2005 Impact of cubic pin finned surface structure geometry upon spray cooling heat transfer *IPACK2005-73003: Proc. IPACK2005, ASME InterPACK'05 (San Francisco, CA)*

[27] Hsieh C-C and Yao S-C 2006 Evaporative heat transfer characteristics of a water spray on micro-structured silicon surfaces *Int. J. Heat Mass Transfer* **49** 962–74

[28] Sodtke C and Stephan P 2007 Spray cooling on micro-structured surfaces *Int. J. Heat Mass Transfer* **50** 4089–97

[29] Li C and Peterson G P 2007 Parametric study of pool boiling on horizontal highly conductive micro-porous coated surfaces *J. Heat Transfer* **129** 1465–75

[30] Sriraman S R and Banerjee D 2007 Pool boiling studies on nano-structured surfaces *IMECE2.007-42581: Proc. IMECE2007 (Seattle, WA)*

[31] Kumar S 2006 Nanofluids—the cooling medium of the future *Heat Transfer Eng.* **27** 1–2

[32] Assael M J, Metaxa I N, Kakosimos K and Constantinou D 2006 Thermal conductivity of nanofluids—experimental and theoretical *Int. J. Thermophys.* **27** 999–1017

[33] Chopkar M 2006 Synthesis and characterization of nanofluid for advanced heat transfer applications *Scr. Mater.* **55** 549–52

[34] Liu M-S 2005 Enhancement of thermal conductivity with
     carbon nanotube for nanofluids *Int. Commun. Heat Mass
     Transfer* **32** 1202–10

[35] Shen J, Graber C, Liburdy J, Pence D V and Narayanan V 2009
     Simultaneous droplet impingement dynamics and heat
     transfer on nano-structured surfaces *Exp. Therm. Fluids Sci.*
     at press (doi:10.1016/j.expthermflusci.2009.02.003)

[36] Bandyopadhyaya R, Nativ-Roth E, Regev O and
     Yerushalmi-Rozen R 2002 Stabilization of individual carbon
     nanotubes in aqueous solutions *Nano Lett.* **2** 25–8

[37] Thiessen D B, Chione D J, McCreary C B and Krantz W B
     2006 Robust digital image analysis of pendant drop shapes
     J. Colloid Interface Sci. **177** 658–65

[38] Woodward R P Surface tension measurements using the drop
     shape method *Technical Guide*
     http://www.firsttenangstroms.com/papers/papers.html

[39] Fordham S 1948 On the calculation of surface tension from
     measurements of pendant drops *Proc. R. Soc.* A **194** 1–16

[40] Hansen F and Rodsrud G 1991 Surface tension by pendant drop
     J. Colloid Interface Sci. **141** 1–9